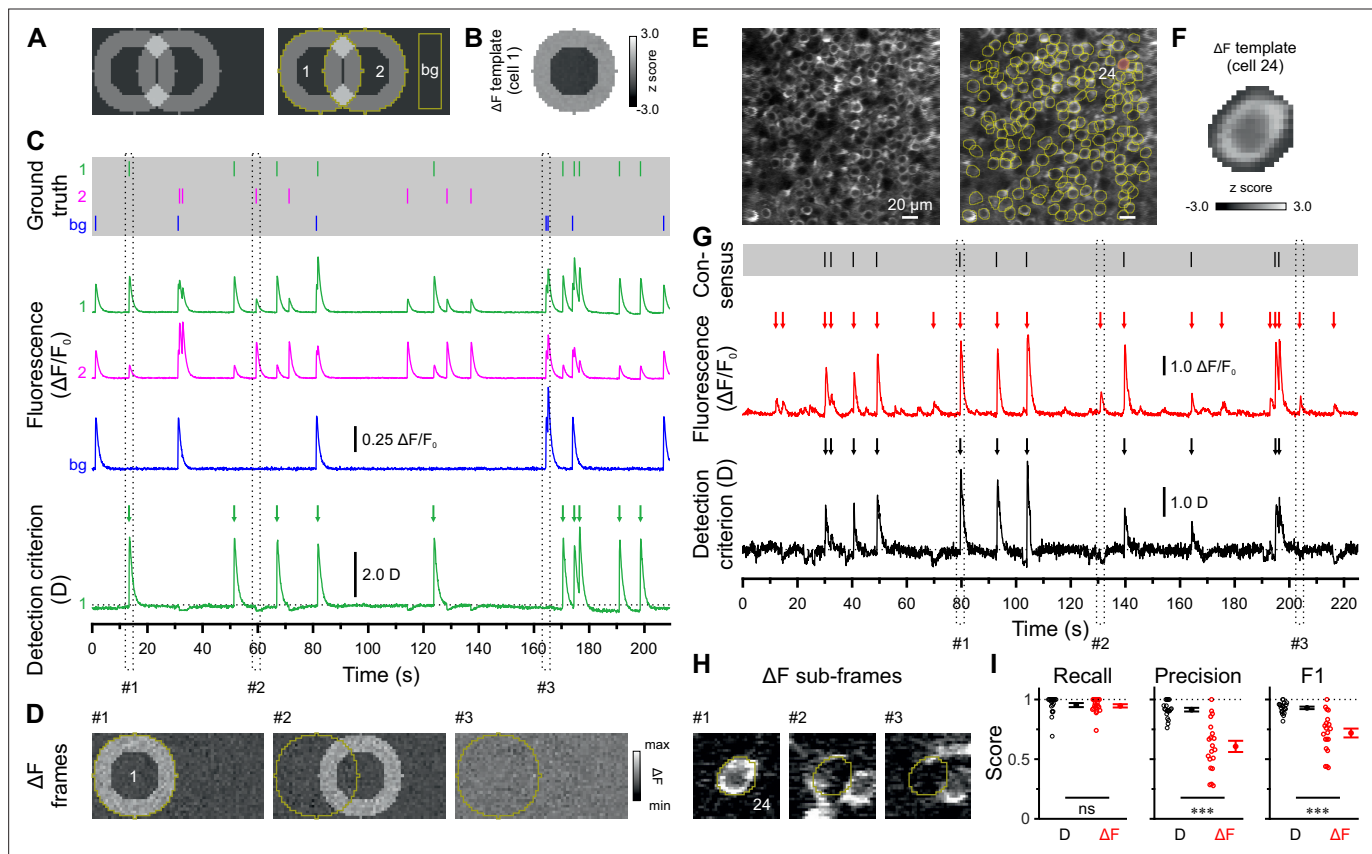


---

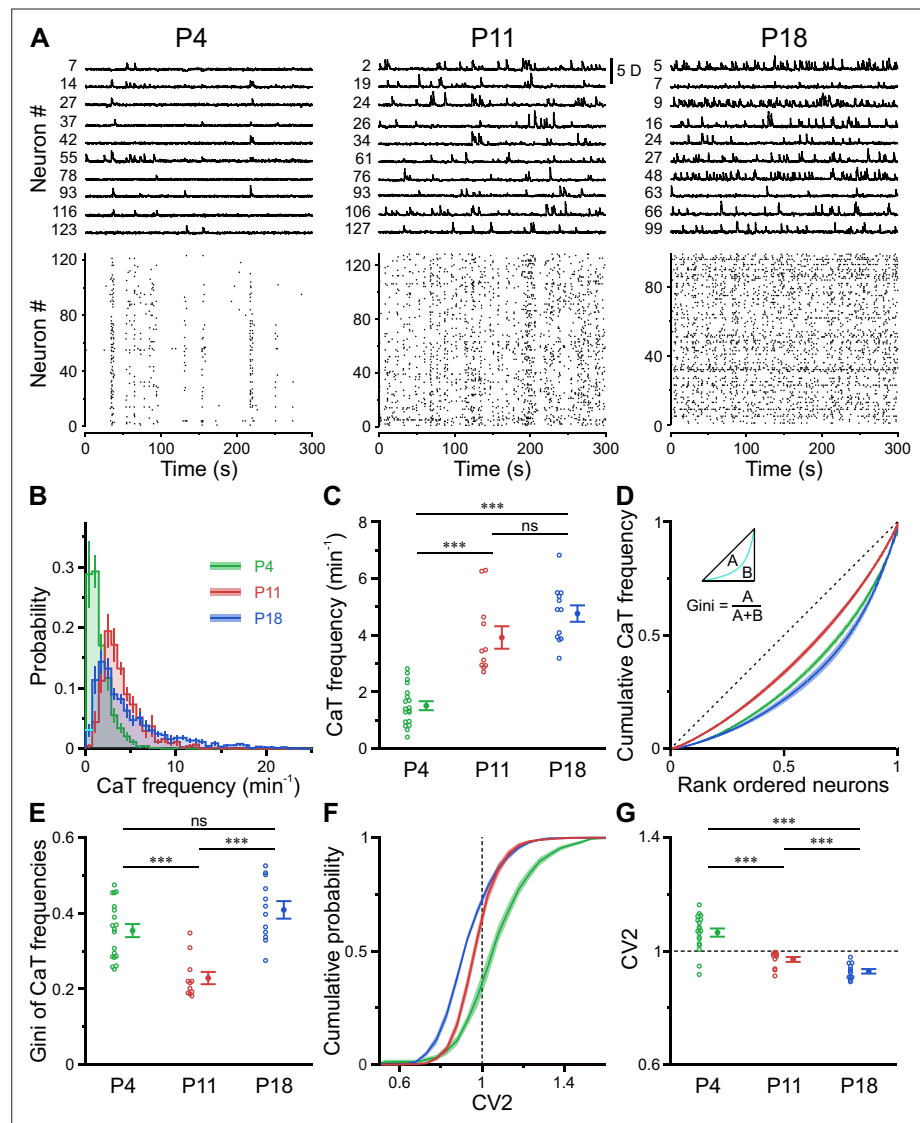
## Figures and figure supplements

Network instability dynamics drive a transient bursting period in the developing hippocampus in vivo

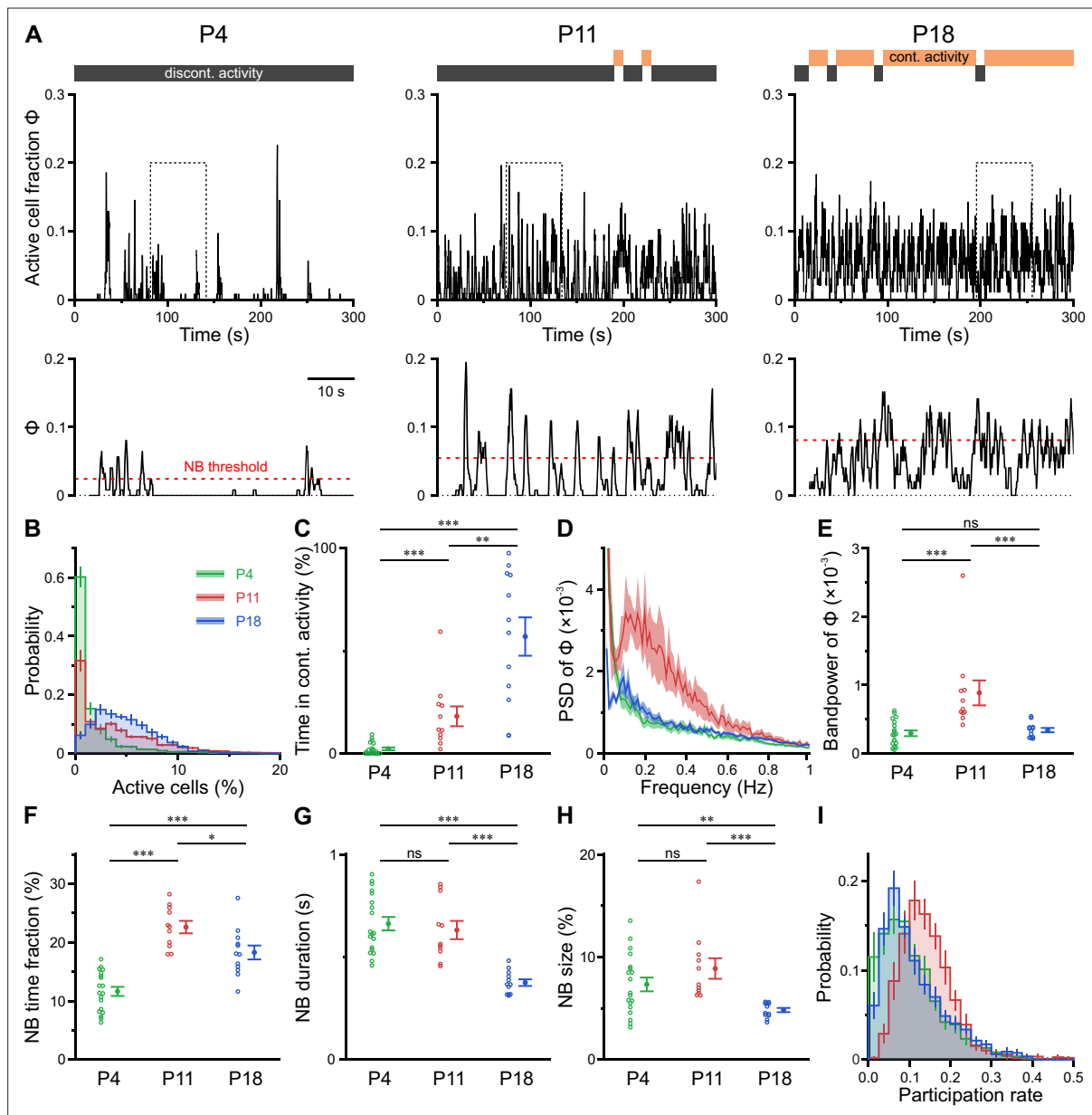
**Jürgen Graf and Vahid Rahmati *et al.***



**Figure 1.** Calcium transient detection harnessing spatial similarity (CATHARSIS) enables reliable  $\text{Ca}^{2+}$  transient (CaT) detection in densely labeled tissue. **(A)** Resting image of two partially overlapping simulated cells (left) and regions of interest (ROIs) used for analysis (right). bg – background. **(B)**  $\Delta F$  template of cell 1. **(C)** Top, simulated trains of action potentials. Middle, relative changes from baseline fluorescence ( $\Delta F/F_0$ ) of ROIs shown in A. Bottom, detection criterion (**D**) for cell 1 and corresponding CaT onsets retrieved by CATHARSIS (arrows). **(D)** Sample  $\Delta F$  images of three individual frames at time points indicated in C. Spikes in cells 1 or 2 translated into ring-shaped increases in  $\Delta F$ , whereas those induced by bg spikes were applied to the entire field of view. **(E)** Resting GCaMP6s fluorescence image (left) and ROIs used for analysis (right). **(F)**  $\Delta F$  template of the cell indicated in E. **(G)** Top, consensus visual annotation by two human experts for the same cell. Middle,  $\Delta F/F_0$  and detected event onsets (red arrows). Bottom, detection criterion (**D**) and corresponding CaT onsets retrieved by CATHARSIS (black arrows). **(H)** Sample  $\Delta F$  images of three individual frames at time points indicated in G. Note that frames #2 and #3 led to false positive results if event detection was performed on mean  $\Delta F$ , but not if performed on D. **(I)** Quantification of recall, precision, and F1 score for event detection based on D (i.e. CATHARSIS) and mean  $\Delta F$ , respectively. Each open circle represents a single cell (n = 20 cells). Data are presented as mean  $\pm$  SEM. ns – not significant. \*\*\* p<0.001. See also **Supplementary file 1a** and **Figure 1—source data 1**.

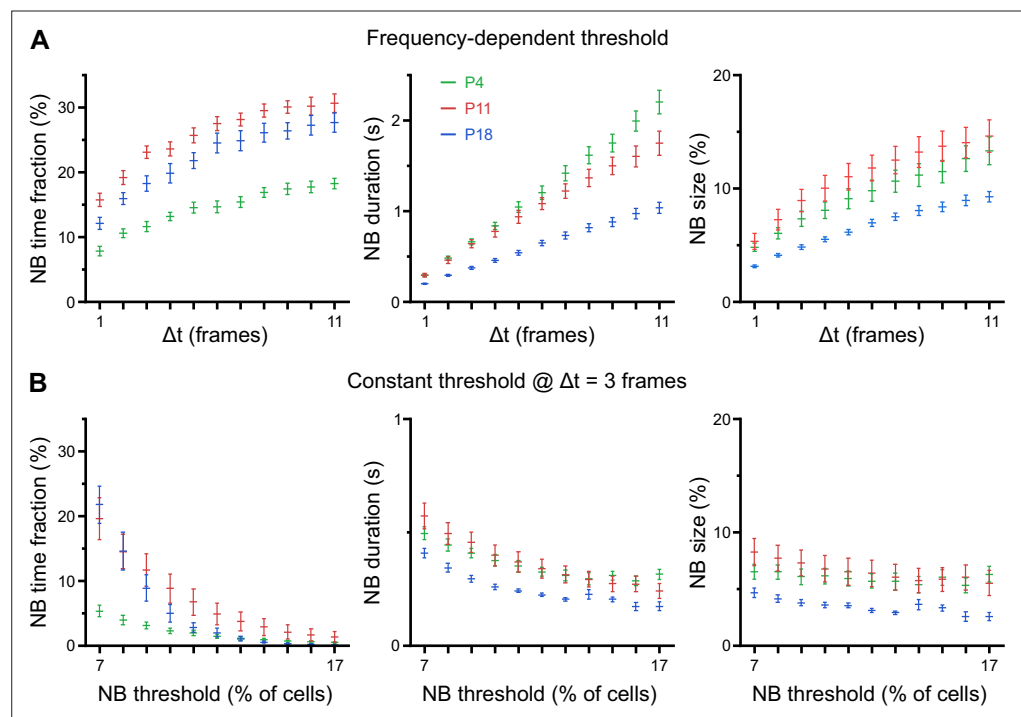


**Figure 2.** A transient period of firing equalization during CA1 development in vivo. **(A)** Sample  $D(t)$  traces (top) and raster plots showing reconstructed  $\text{Ca}^{2+}$  transient (CaT) onsets (bottom). Note the developmental transition from discontinuous to continuous network activity. **(B)** Empirical probability distribution of CaT frequencies. **(C)** Mean CaT frequencies per field of view (FOV). **(D)** Lorenz curves of CaT frequencies. Line of equality (dotted) represents the case that all neurons have equal CaT frequencies. Inset depicts Gini coefficient calculation. **(E)** Mean Gini coefficients per FOV. **(F)** Cumulative probability of mean coefficient of variation (CV2) of inter-CaT intervals. Note that, at P11, CV2 distribution is narrower and centered around 1. **(G)** Mean CV2 per FOV. For a Poisson process, CV2 = 1 (dotted line). Each open circle represents a single FOV. Data are presented as mean  $\pm$  SEM. ns – not significant. P4: P3–4,  $n = 19$  FOVs from six mice, P11: P10–12,  $n = 11$  FOVs from six mice, P18: P17–19,  $n = 12$  FOVs from six mice, and \*\*\*  $p < 0.001$ . See also **Supplementary file 1b** and **Figure 2—source data 1**.

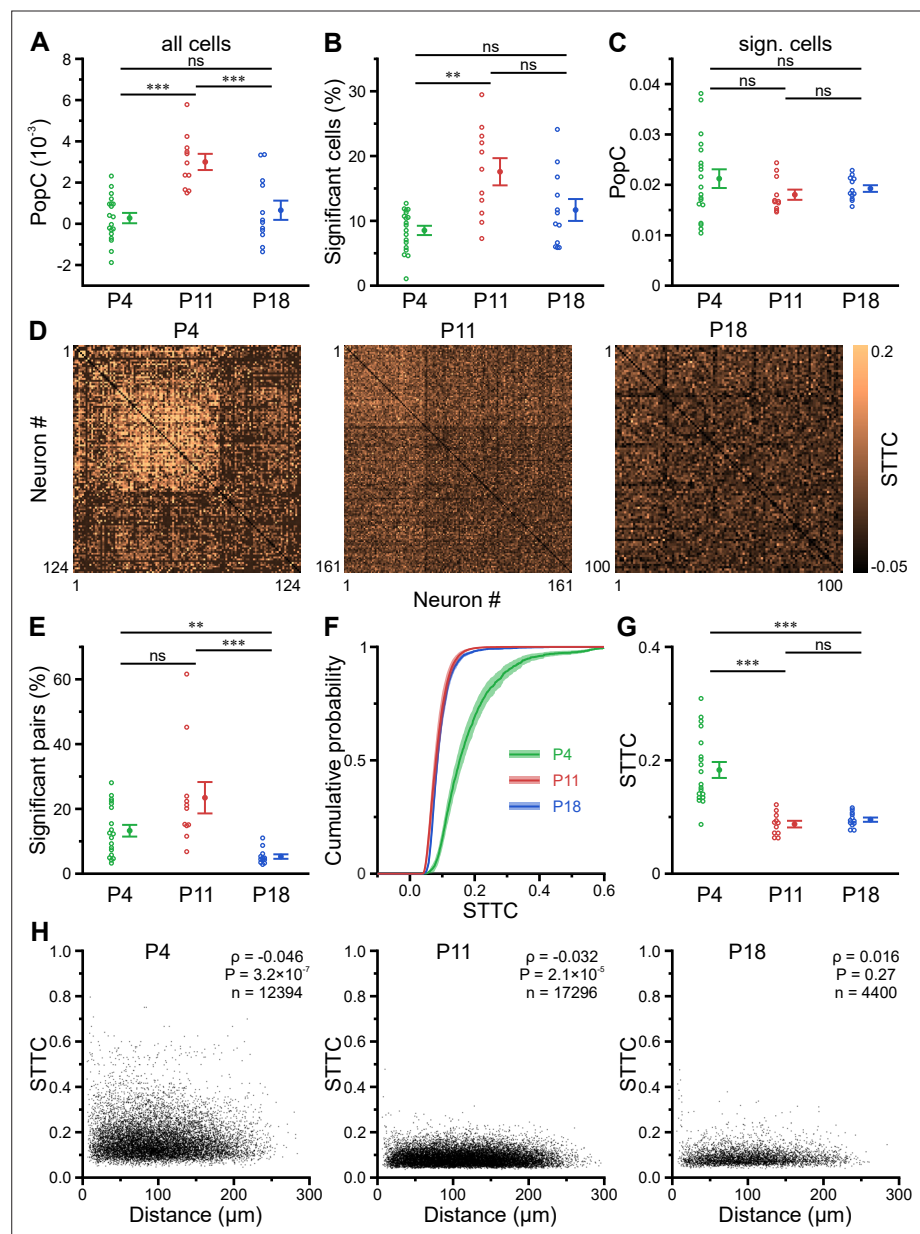


**Figure 3.** CA1 undergoes a transient enhanced bursting period while progressively transitioning from discontinuous to continuous activity. **(A)** Sample traces of the fraction of active cells  $\Phi(t)$ . Gray and orange bars indicate discontinuous and continuous network activity, respectively. Bottom traces show time periods marked on top (dotted rectangle) at higher temporal resolution. Red dotted lines indicate the activity-dependent thresholds for network burst (NB) detection. **(B)** Empirical probability distribution of active cells per frame. **(C)** Continuous activity emerges at P11 and dominates over discontinuous activity at P18. **(D)** Power spectral density of  $\Phi(t)$ . **(E)** Bandpower of  $\Phi(t)$  in the 0.1–0.5 Hz range. **(F)** The fraction of time that the network spends in NBs peaks at P11. **(G)** The average NB duration is lowest at P18. **(H)** Quantification of NB size as the mean fraction of active neurons (corrected for NB threshold as indicated in A). **(I)** Empirical probability distribution of the fraction of NBs that each cell is participating in. Each open circle represents a single field of view (FOV). Data are presented as mean  $\pm$  SEM. ns – not significant. P4: P3–4, P11: P10–12, P18: P17–19, \*\*\*  $p < 0.001$ , \*\*  $p < 0.01$ , and \*  $p < 0.05$ . See also **Supplementary file 1c** and **Figure 3—source data 1**.

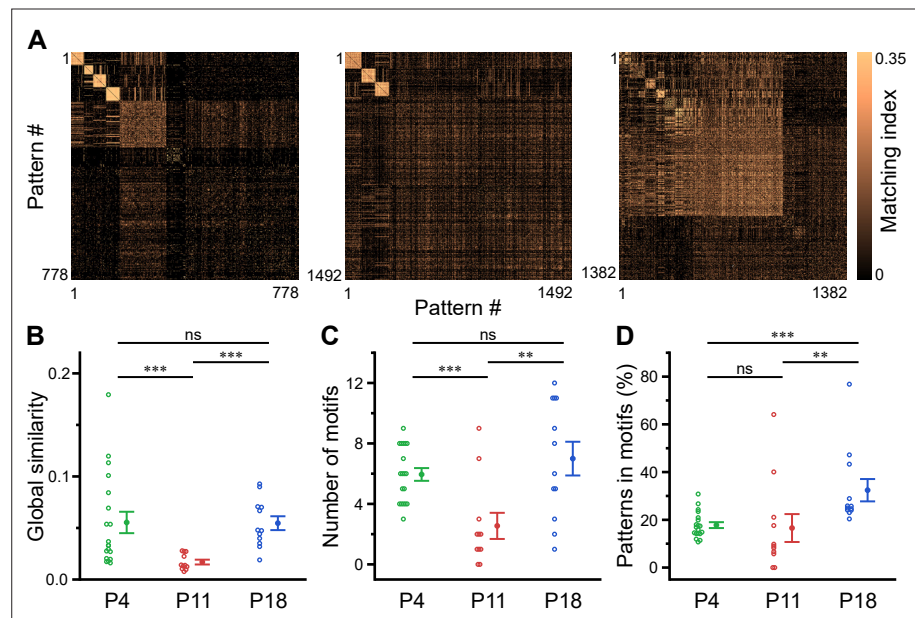




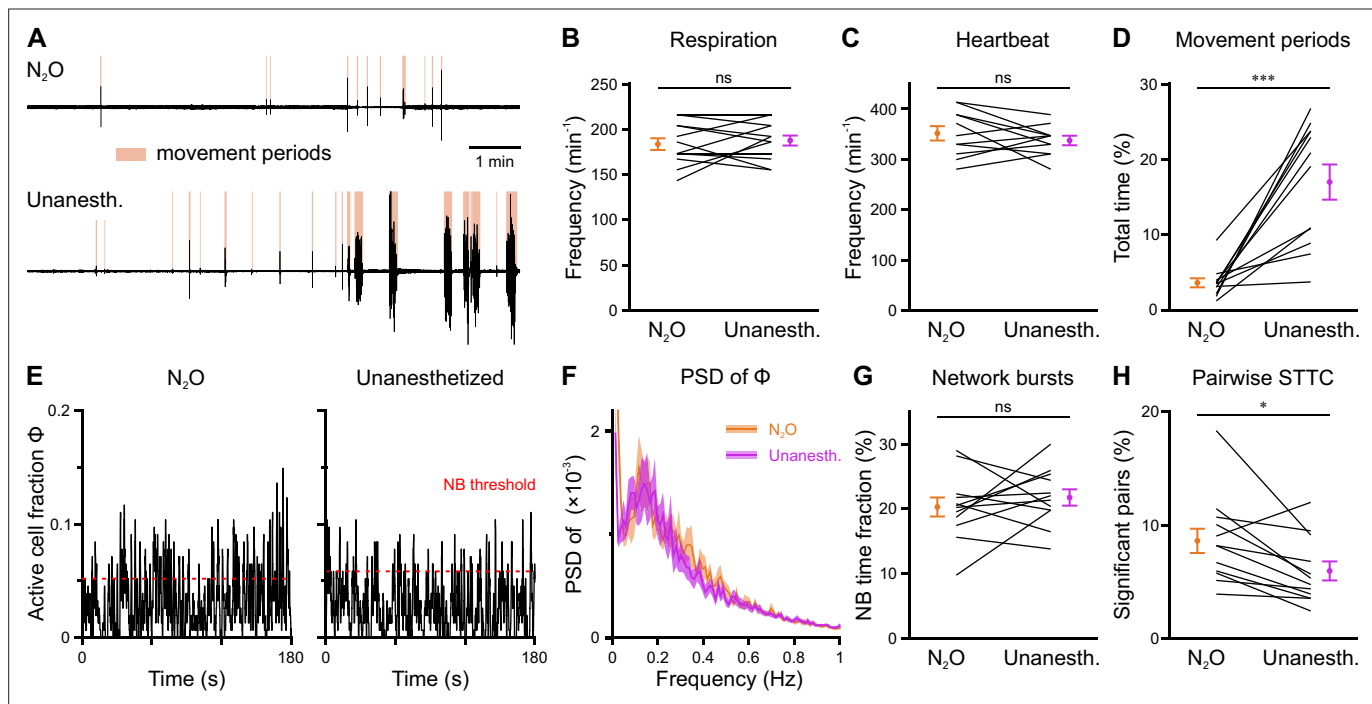
**Figure 3—figure supplement 1.** Developmental changes in network burst (NB) characteristics are robust to a wide range of definitions. **(A)** Total time spent in NBs (left), mean NB duration (middle), and mean NB size (right) as a function of the parameter  $\Delta t$ .  $\Delta t$  was used for computing a  $\text{Ca}^{2+}$  transient (CaT) frequency-dependent threshold, separately for each field of view (FOV; see Methods for details). Sampling rate was 11.63 Hz. **(B)** Total time spent in NBs (left), mean NB duration (middle), and mean NB size (right) as a function of a constant threshold applied to all FOVs, i.e., independent of CaT frequencies. Note that threshold values below  $\sim 10\%$  are less meaningful, as the average fraction of active cells in some FOVs at P18 is  $\sim 9\%$ . More generally, for a constant threshold applied to all FOVs, highly active FOVs will be biased toward higher false-positive NB rates, whereas less active FOVs will be biased toward higher false-negative NB rates.  $\Delta t$  was set to 3. See also **Figure 3—figure supplement 1—source data 1**.



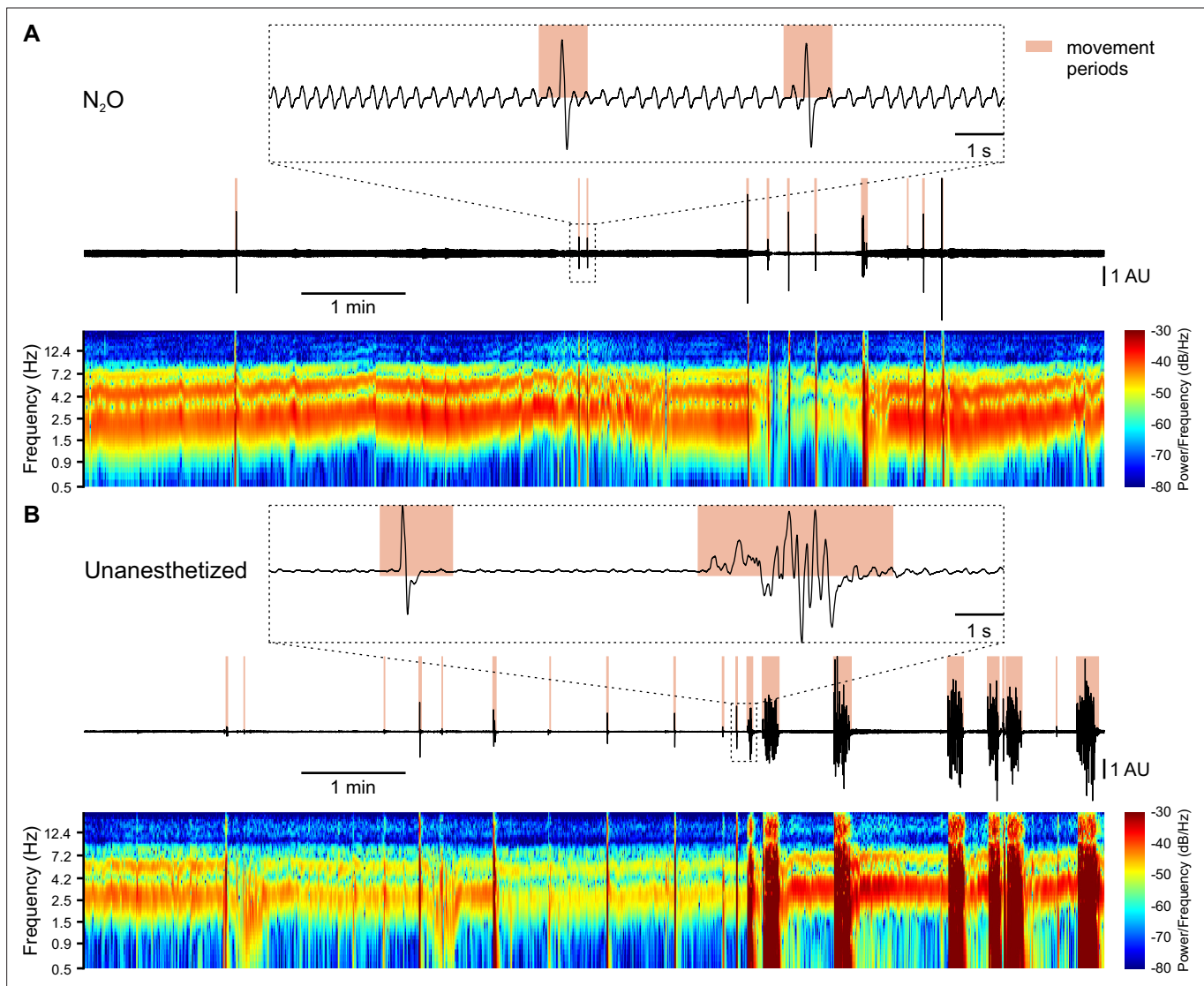
**Figure 4.** Enhanced population coupling (PopC) underlies network burstiness in the second postnatal week in vivo. **(A)** The mean PopC index peaked at P11. **(B)** Mean fraction of cells with significant PopC. **(C)** Mean PopC index of significantly coupled cells only. **(D)** Sample spike-time tiling coefficient (STTC) matrices (re-ordered) from three individual fields of view (FOVs) at P4, P11, and P18. **(E)** Mean fraction of cell pairs having a significant STTC. **(F)** Cumulative probability of STTCs of significantly correlated cell pairs only. **(G)** Mean STTCs of significantly correlated cell pairs. **(H)** Relationship between STTC and Euclidean somatic distance for significantly correlated cell pairs.  $\rho$  denotes the Spearman's rank correlation coefficient for all cell pairs analyzed ( $n$ ) at a given age. **(A–C and E–G)** Each open circle represents a single FOV. Data are presented as mean  $\pm$  SEM. ns – not significant. P4: P3–4, P11: P10–12, P18: P17–19, \*\*\*  $p < 0.001$ , and \*\*  $p < 0.01$ . See also **Supplementary file 1d** and **Figure 4—source data 1**.



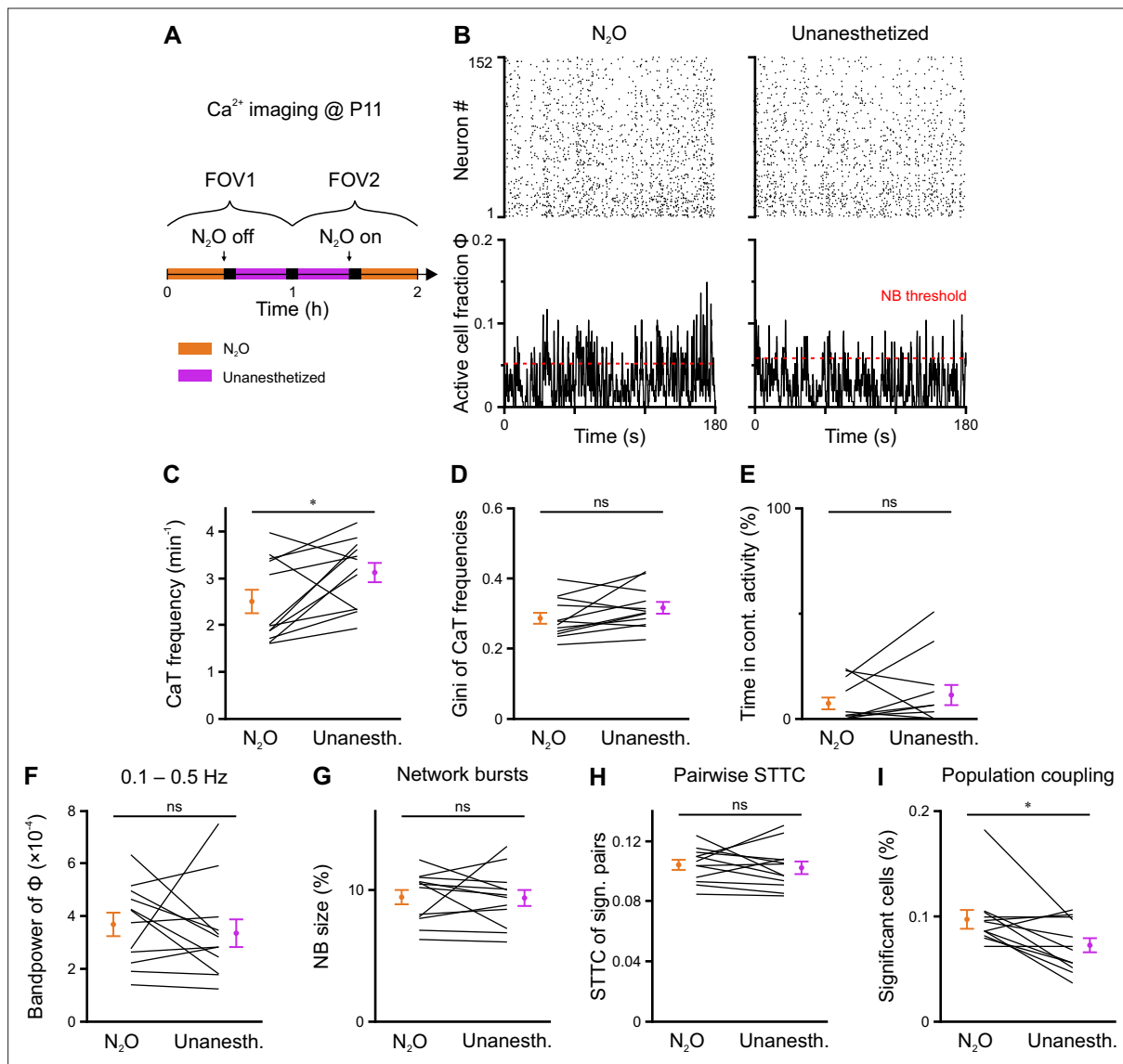
**Figure 5.** Motifs of CA1 network activity undergo distinct developmental alterations. **(A)** Similarity matrices (matching index) of binary activity patterns (re-ordered for illustration of motif detection) from three individual fields of view (FOVs) at P4, P11, and P18. **(B)** Global similarity of activity patterns is lowest at P11. **(C)** The absolute number of detected motifs per FOV is lowest at P11. **(D)** Motif repetition quantified as the fraction of activity patterns belonging to each motif. Each open circle represents a single FOV. Data are presented as mean  $\pm$  SEM. ns – not significant. P4: P3–4, P11: P10–12, P18: P17–19, \*\*\*  $p < 0.001$ , and \*\*  $p < 0.01$ . See also **Supplementary file 1e** and **Figure 5—source data 1**.



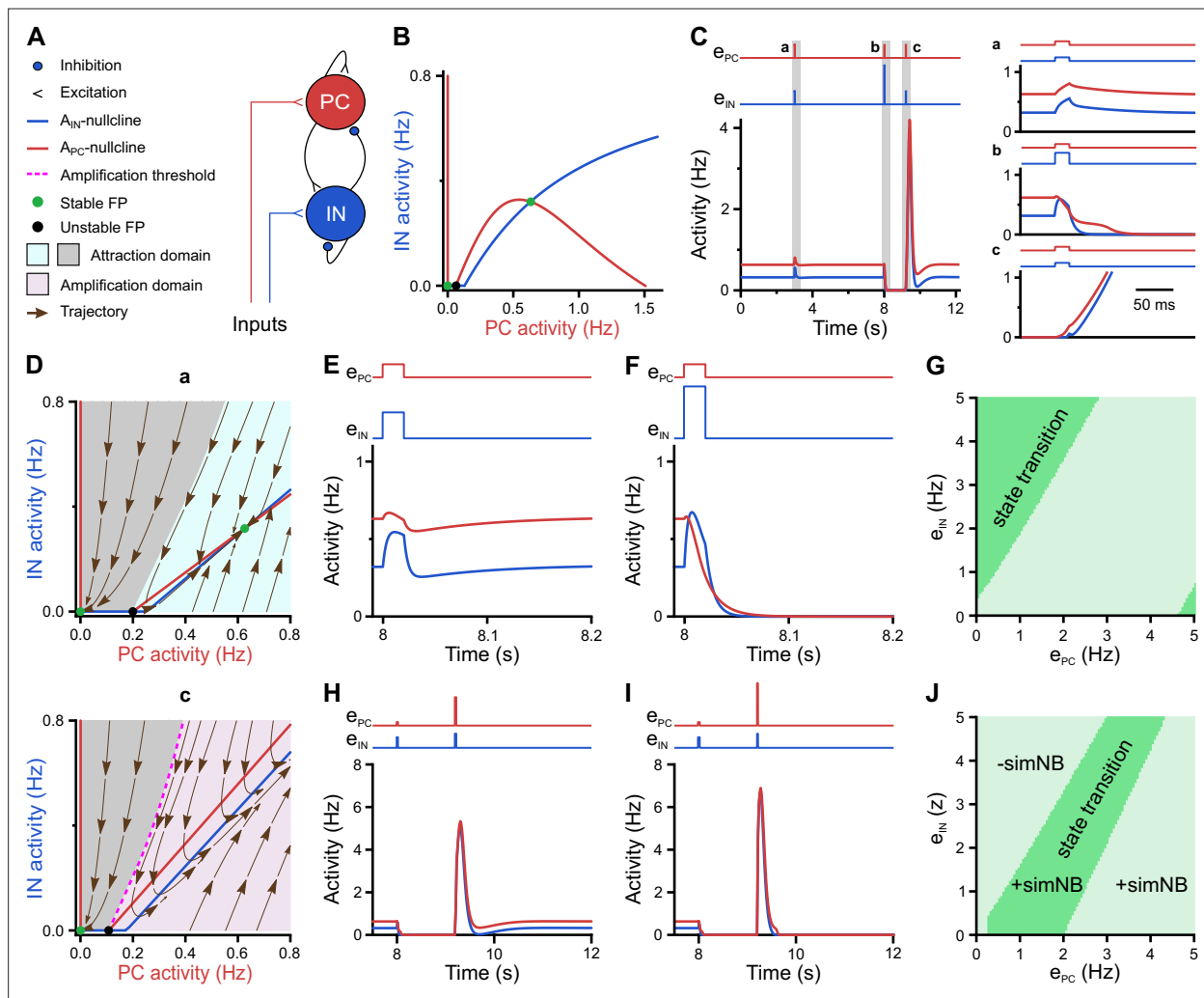
**Figure 6.** Effects of nitrous oxide ( $N_2O$ ) on body movements, vital parameters, and network activity at P11. **(A)** Sample respiration/movement signal from an individual mouse receiving either 75%  $N_2O$ /25%  $O_2$  (top) or pure  $O_2$  (Unanesth., bottom). Detected movement periods are highlighted. **(B)** Respiration rate is unaffected by  $N_2O$  ( $n = 12$  fields of view [FOVs] from six mice). **(C)** Heart rate is unaffected by  $N_2O$  ( $n = 11$  FOVs; in the recording from one FOV, heart rate could not be reliably determined). **(D)**  $N_2O$  significantly reduces movement periods. **(E)** Sample traces of the fraction of active cells  $\Phi(t)$  ( $\Delta t = 3$  frames). Red dotted lines indicate the activity-dependent thresholds for network burst (NB) detection. **(F)** Power spectral density of  $\Phi(t)$  is similar in the presence or absence of  $N_2O$ . **(G)** The fraction of time that the network spends in NBs. **(H)** Fraction of neuron pairs having a significant spike-time tiling coefficient (STTC). Data are presented as mean  $\pm$  SEM. ns – not significant. \*\*\*  $p < 0.001$  and \*  $p < 0.05$ . See also **Supplementary file 1f** and **Figure 6—source data 1**.



**Figure 6—figure supplement 1.** Detection of body movements, breathing, and heart rate. **(A and B)** Sample respiration/movement signal (middle) and time-aligned spectrogram (bottom; 0.5–20 Hz, window length: 1 s, overlap: 50%) used to detect movement periods, respiration, and heart rate. Top: marked time periods (dotted rectangle) at higher temporal resolution. Signals were recorded by means of a pressure sensor positioned below the chest of the animal. **(A)** Recording from an animal receiving 75%  $N_2O$ /25%  $O_2$  (' $N_2O$ '). **(B)** Recording from the same mouse receiving pure oxygen ('Unanesthetized').

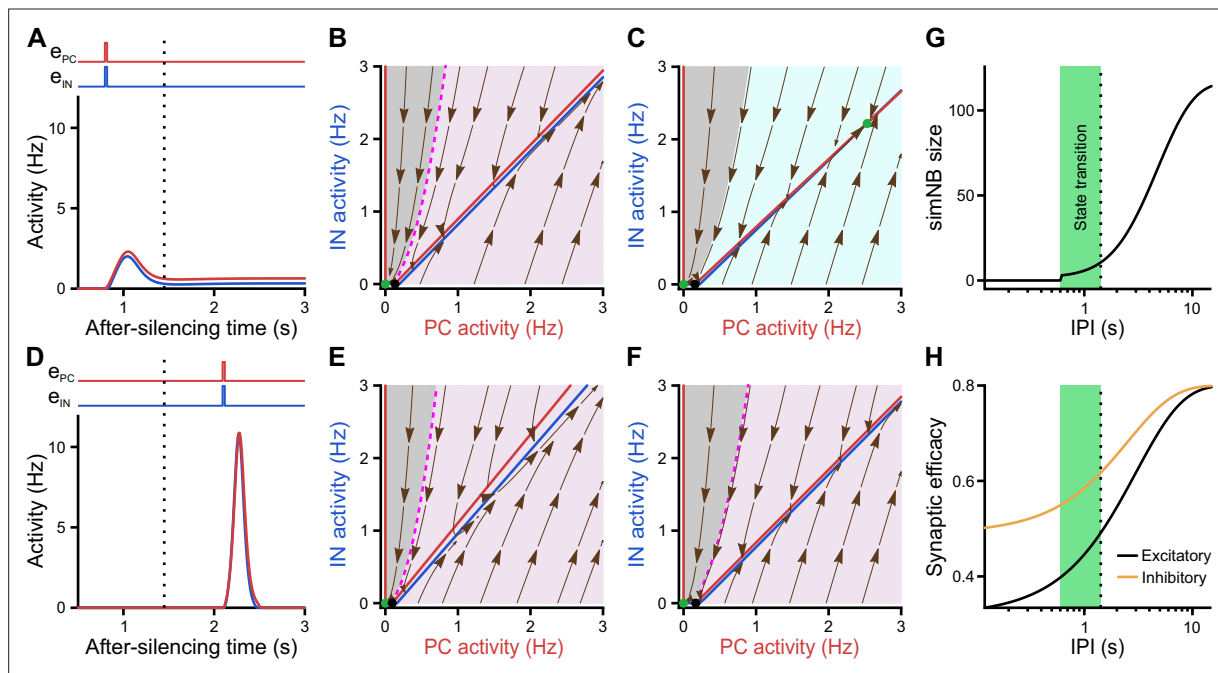


**Figure 6—figure supplement 2.** Effects of nitrous oxide on CA1 network dynamics at P11. **(A)** Experimental timeline. In each animal, two fields of view (FOVs) were recorded with and without  $\text{N}_2\text{O}$  (paired design). **(B)** Rasterplots (top) and time-aligned fraction of active cells  $\Phi(t)$  (bottom) from the same FOV in either the presence or the absence of  $\text{N}_2\text{O}$ . Red dotted lines indicate the activity-dependent thresholds for network burst (NB) detection. **(C)** Mean  $\text{Ca}^{2+}$  transient (CaT) frequency per FOV. **(D)** Mean Gini coefficients of CaT frequencies per FOV. **(E)** Percentage of time spent in continuous activity. **(F)** Bandpower of  $\Phi(t)$  in the 0.1–0.5 Hz range. **(G)** NB size quantified as the mean fraction of active neurons per NB (corrected for burst threshold as indicated in B). **(H)** Mean spike-time tiling coefficient (STTC) of significantly correlated cell pairs. **(I)** Mean fraction of cells with significant population coupling (PopC).  $n = 12$  FOVs from six mice, \*  $p < 0.05$ , and ns – not significant. See also **Supplementary file 1f** and **Figure 6—source data 1**.



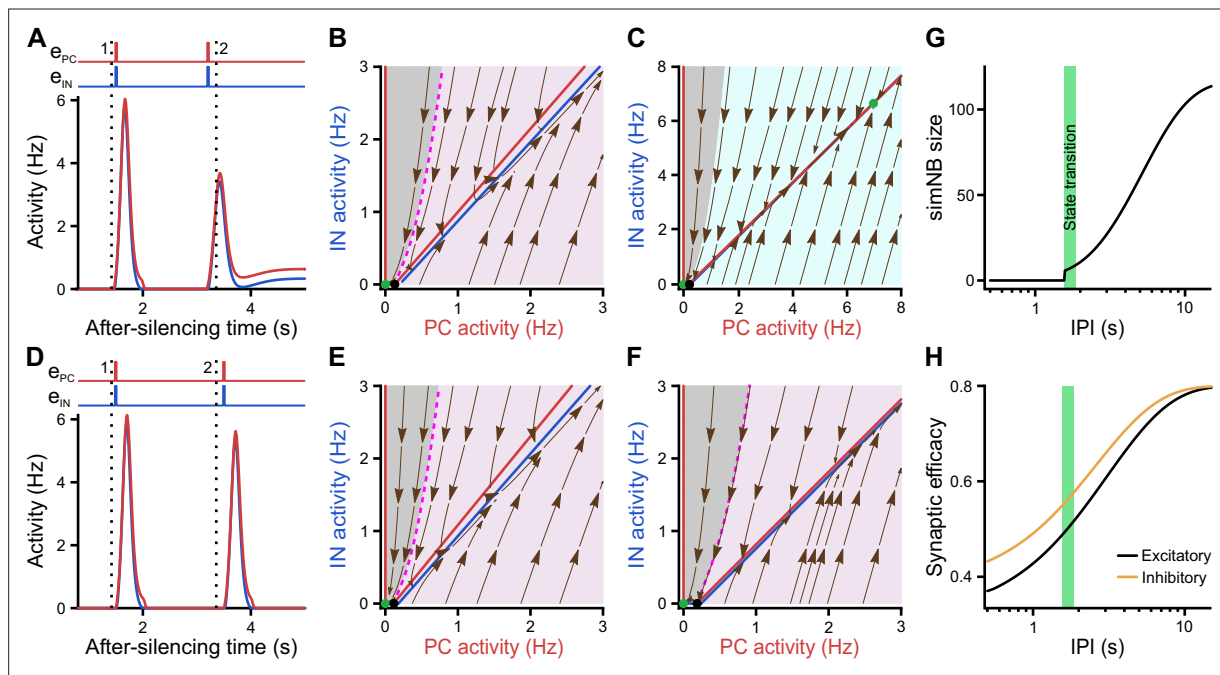
**Figure 7.** A neural network model with inhibitory GABA identifies intrinsic instability dynamics as key to the emergence of network bursts. **(A)** Schematic diagram of the short-term synaptic plasticity (STP)-recurrent neural network (RNN) model. **(B)** The  $A_{IN}$ - $A_{PC}$ -plane of the full STP-RNN's stationary dynamics. Note the presence of two stable fixed points (FPs; green dots) at silent and active states as well as the unstable FP (black dot). **(C)** Simulated network burst (simNB) generation requires network silencing. The model was stimulated by pulse-like input to both pyramidal cell (PC) and interneuron (IN) populations for a duration of 0.020 s (at  $t = 3$  and  $9.2$  s:  $e_{PC} = e_{IN} = 0.25$ ; at  $t = 8$  s:  $e_{PC} = 0.25$ ,  $e_{IN} = 0.75$ ). Zoom-in of the activity around the stimulation times at active (a and b) and silent (c) states is shown in right panels. Input time series are shown on top of the plots. **(D)** The presence of an amplification domain in the initial phase of network firing dynamics enables the emergence of simNBs. The  $A_{IN}$ - $A_{PC}$ -plane of the STP-RNN with synaptic efficacies frozen at active (a, top) and silent (b, bottom) states, right before input arrival. **(E–G)** Transition from active to silent state requires specific input ratios. Input delivered at  $t = 8$  s. **(E)** A failed transition:  $e_{PC} = 0.25$ ,  $e_{IN} = 0.5$ . **(F)** A successful transition:  $e_{PC} = 0.25$ ,  $e_{IN} = 1$ . **(G)** A color-coded matrix of successful (dark green) and failed (light green) transitions to the silent state in response to different combinations of  $e_{PC}$  and  $e_{IN}$  amplitudes. **(H–J)** Both the transition from the silent to the active state and the simNB generation require specific input ratios. Input delivered at  $t = 9.2$  s. Same as **E–G**, but for the backward transition to the active state. +simNB and -simNB indicate the emergence and absence of bursts.





**Figure 8.** Internal deadline of state transitions. (A–C) Input delivered to the network before the deadline can move it to active state. (A) A successful transition. The input delivered at  $t = 0.8$  s;  $e_{PC} = 0.25$ ,  $e_{IN} = 0.25$ . (B) The  $A_{IN}$ - $A_{PC}$ -plane of the short-term synaptic plasticity (STP)-recurrent neural network (RNN) with synaptic efficacies frozen at the silent state right before the input arrival. (C) Same as B, but frozen at the peak of the network burst (i.e. simulated network burst [simNB]) shown in A. Note the presence of the transient stable fixed point (FP; non-origin green dot), which triggers the transitioning to the active state. (D–F) Once the deadline is missed, the network cannot be moved to the active state by the subsequent input. Same as A–C, but the input delivered at  $t = 2.1$  s. Note the absence of a non-origin transient stable FP in F, in contrast to C. (G) The simNB size and network transition to the active state depend on the inter-pulse intervals (IPIs: the arrival time of the next input relative to the silencing time of the network). simNB size is computed as the maximum of  $A_{IN} + A_{PC}$  after the secondary input. Note the presence of a short window for transitioning to the active state.  $e_{PC} = 0.25$ ,  $e_{IN} = 0.25$ . (H) Same as G, but for the non-scaled efficacies of GABAergic ( $u_{IXI}$ ; orange; see Methods) and glutamatergic ( $u_{IXP}$ ; black) synapses, right before the arrival of the secondary input. (A, D, G, and H) The dotted line at  $t = 1.45$  s depicts the internal deadline.





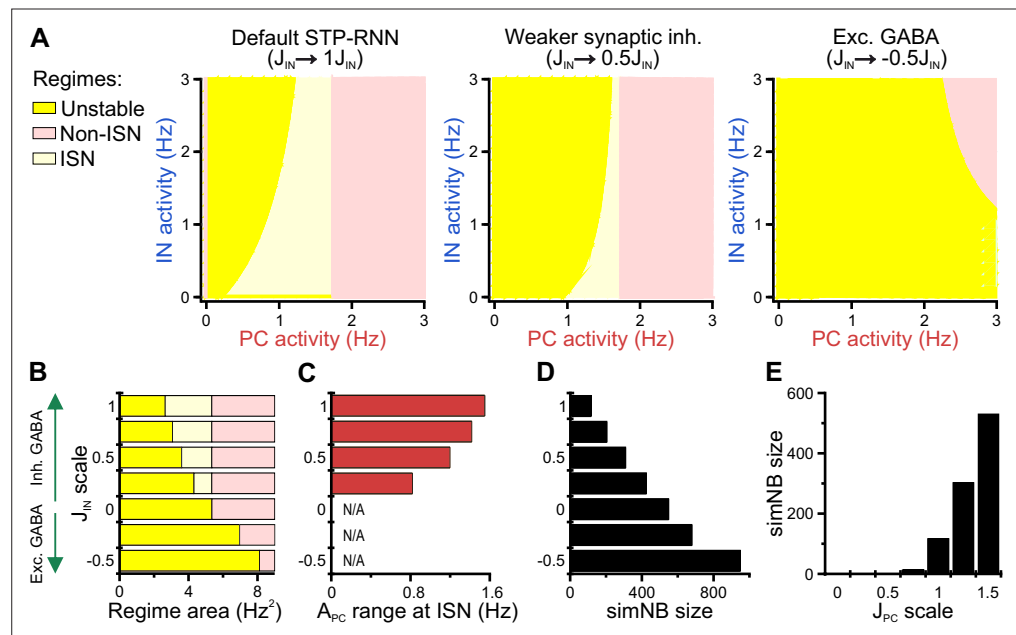


**Figure 9.** Inhibitory stabilization of a persistent active state in the bi-stable short-term synaptic plasticity (STP)-recurrent neural network (RNN) model. **(A)** The inhibition-stabilized network (ISO) regime becomes accessible to the network upon the developmental emergence of synaptic inhibition. The colored regions in each  $A_{IN}$ - $A_{PC}$ -plane of the network model depict the fixed point (FP)-domains of three possible operating regimes: unstable dynamics, ISO, and Non-ISO. Synaptic inhibition strength  $J_{IN}$  was set to 3 (inhibitory; left), 1.5 (inhibitory, middle), and -1.5 (excitatory, right). **(B–D)** Effect of strength and polarity of GABAergic synapses ( $J_{IN}$ ) on the availability of the ISO regime **(B)**, the maximum range of pyramidal cell (PC) activity in the ISO regime **(C)**, and size of simulated network bursts (simNBs) when triggered at the rest state **(D)**. Results were obtained by scaling  $J_{IN}$  in the STP-RNN model with values indicated on the y-axis. The area of each operating regime was computed based on the area of its FP-domain in the  $A_{IN}$ - $A_{PC}$ -plane (with limits as in A). **(E)** Dependency of simNB size on the strength of glutamatergic synapses ( $J_{PC}$ ). Default value of  $J_{PC}$  in STP-RNN was 6.5 (corresponding to a scale of 1).

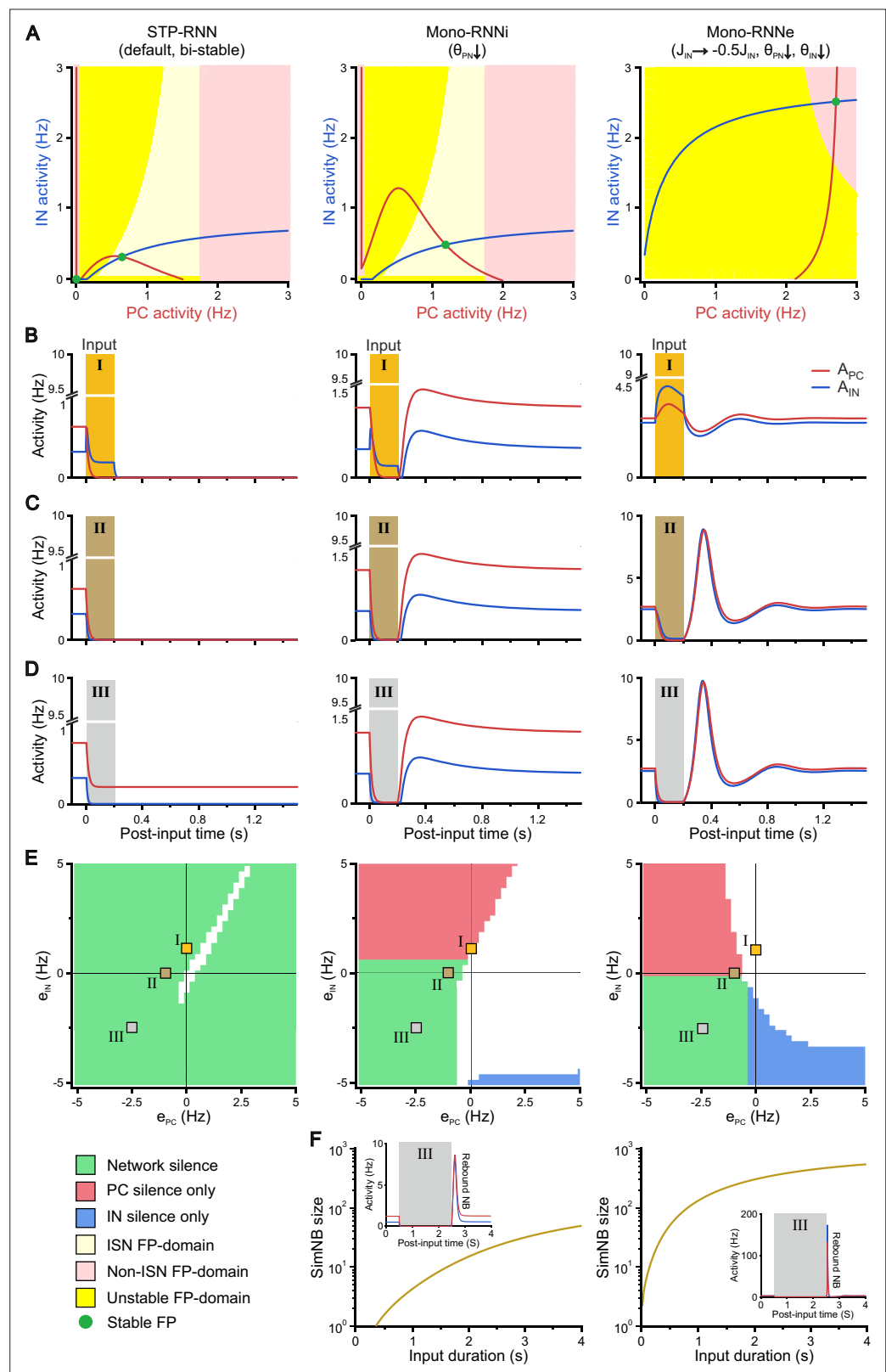


**Figure 9—figure supplement 1.** A bi-stable short-term synaptic plasticity (STP)-recurrent neural network (RNN) model with inhibitory GABA robustly explains the experimental observations. **(A)** In contrast to the bi-stable STP-RNN, Mono-RNNi and Mono-RNNe networks lack a silent state (i.e. a fixed point [FP] at origin). Same format as **Figure 9A**, overlaid by the  $A_{PC}$ -nullcline (red), the  $A_{IN}$ -nullcline (blue), and the FPs of each network with dynamic Figure 9—figure supplement 1 continued on next page

Figure 9—figure supplement 1 continued

synapses (i.e. 10D system). The unstable FP in the STP-RNN is not shown for clarity. For the exact values of model parameters, see Methods. **(B–C)** Network responses to example inputs (200 ms; shaded areas). In contrast to the STP-RNN, Mono-RNNi and Mono-RNNe networks can be silenced only during the input. Inputs are:  $e_{PC}=0$ ,  $e_{IN}=1$  **(B)**;  $e_{PC}=-1$ ,  $e_{IN}=0$  **(C)**;  $e_{PC}=e_{IN}=-2.5$  **(D)**. **(E)** In contrast to the STP-RNN, silencing of Mono-RNNi and Mono-RNNe models requires the input (200 ms) to at least one of network populations to be inhibitory. Green indicates complete network silence ( $A_{PC}=A_{IN}=0$ ), red indicates pyramidal cell (PC) silence only ( $A_{PC}=0$ ,  $A_{IN}\neq 0$ ), and blue indicates interneuron (IN) silence only ( $A_{PC}\neq 0$ ,  $A_{IN}=0$ ). White areas:  $A_{PC}\neq 0$ ,  $A_{IN}\neq 0$ . The activity levels of the neuronal populations were computed as those prior to the input removal. Square symbols (I–III) indicate the input combinations used in panels **B–D**. **(F)** In contrast to the STP-RNN, effective (rebound) simulated network burst (simNB) generation in Mono-RNNi (middle) and Mono-RNNe (right) requires a relatively long-lasting input. (Inset) Same as **D**, but for a longer input of 2 s.